Journal of
Materials Chemistry A

ROYAL SOCIETY
OF CHEMISTRY

PAPER

View Article Online
View Journal

Check for updates

Cite this: DOI: 10.1039/d6ta02355j

Phosphate buffer-induced depletion of nickel redox sites limits oxygen evolution on stainless steel anodes

Kiho Nishioka, * Sakino Hiro and Kuniaki Murase *

Although water electrolysis at neutral to mildly alkaline pH (7–12) expands the range of applicable cell components, pH fluctuations and mass transport limitations can hinder high-efficiency operation at high current densities. Phosphate buffer systems mitigate pH variations and therefore are considered promising electrolytes for such systems; however, their unrecognized chemical impact on electrode materials remains a critical bottleneck. Here, we systematically investigate the oxidation of 304 stainless steel (304 SS) anodes and its impact on the oxygen evolution reaction (OER) in phosphate-buffered electrolytes. The data demonstrate that the electrode surface generated in phosphate electrolytes is fundamentally different from that formed in KOH. The SS surface formed in phosphate electrolytes leads to an irreversible decrease in OER activity due to the depletion of nickel-based electrochemically redox-active sites. In contrast, KOH electrolytes readily form and maintain an active layer primarily comprising nickel species, enabling the full recovery of both redox capacity and OER activity even for electrodes previously deactivated in phosphate electrolytes. Notably, rather than adsorption, phosphate in the electrolytes induces the selective dissolution of nickel and iron to a depth of approximately four to six monolayers, resulting in the depletion of redox-active sites. These findings reveal intrinsic limitations of phosphate-based electrolytes for OER catalysts relying on nickel redox-active sites. The present results also highlight the importance of considering complexation-induced metal dissolution in electrolyte design and assessing the interfacial chemistry of redox-driven transition metal catalytic systems in general.

Received 19th March 2026
Accepted 3rd May 2026

DOI: 10.1039/d6ta02355j

rsc.li/materials-a

Introduction

Water electrolysis is a promising means of producing green hydrogen using renewable energy but improvements in efficiency and reductions in cost are both required.[1–4] In recent years, the commercialization of the alkaline water electrolysis (AWE) process has accelerated because, in principle, this technology can operate using less expensive and more earth-abundant materials compared with polymer electrolyte membrane water electrolysis, which functions under strongly acidic conditions.[5] Unfortunately, conventional AWE systems employ highly concentrated alkaline electrolytes that can lead to the corrosion and degradation of system components. Hence, AWE processes require membrane materials and cell components that are resistant to alkaline environments.[6,7] These special requirements remain a major obstacle to further reductions in the cost of AWE systems.

Considering these challenges, water electrolysis systems operating under neutral to mildly alkaline conditions (pH 7–12) have recently been explored. However, challenges remain with regard to the oxygen evolution reaction (OER) occurring at the counter electrode. During the OER in an AWE process, OH^- ions are oxidized according to the reaction, $4OH^- \rightarrow O_2 + 4H^+ + 4e$. At neutral to mildly alkaline pH values, the activity (that is, the effective concentration) of OH^- ions is low and so the progress of the OER rapidly becomes limited by the rate of diffusion. As a result, stable operation at high current densities with low OER overpotentials becomes difficult.[8] As an example, in the case that 0.1 mol kg^{-1} $NaClO_4$ is used as the supporting electrolyte, a diffusion-limited current related to OH^- oxidation that is not observed at pH $\geq$ 12 becomes apparent at pH 11.[9] In addition, pH gradients can form between the cathode and anode and induce an overpotential loss of approximately 60 mV per pH unit according to the Nernst equation, thereby reducing the overall water electrolysis efficiency.[10] Achieving high-efficiency electrolysis at high current densities with neutral to mildly alkaline pH values will require the design of electrolytes having high buffering capacities that can effectively suppress pH fluctuations in the vicinity of the electrodes.

Accordingly, the applicability of buffered electrolytes based on polyprotic acids, the pH of which can be adjusted from neutral to alkaline, has been actively investigated in recent years.[11–16] In particular, buffer systems based on phosphoric acid, a triprotic acid, have been found to effectively suppress pH fluctuations

---

Department of Materials Science and Engineering, Kyoto University, Sakyo-ku, Kyoto 606-8501, Japan. E-mail: nishioka.kiho.2h@kyoto-u.ac.jp; murase.kuniaki.2n@kyoto-u.ac.jp

associated with electrode reactions by supplying either H^+ or OH^- depending on the local reaction environment. As an example, using K_2HPO_4 as the buffer salt involves the reactions

$$HPO_4^{2-} + H^+ \rightleftharpoons H_2PO_4^- \quad (1)$$

as a source of H^+ and

$$HPO_4^{2-} + OH^- \rightleftharpoons PO_4^{3-} + H_2O \quad (2)$$

as a source of OH^-. HPO_4^{2-} can thus function as either an acid or a base *via* these buffer pairs, depending on the reaction conditions, thereby stabilizing the pH in the vicinity of the electrode.

It has recently been reported that the formation of oxide/hydroxide films containing nickel and iron on stainless steel (SS) surfaces leads to high OER catalytic activity in KOH electrolytes.[17–19] SS is relatively inexpensive, is composed of earth-abundant elements, and has a surface oxide nanostructure that can be tailored depending on the electrochemical conditions. As such, this metal is an attractive candidate for the manufacture of binder-free, highly durable electrode catalysts. In particular, it has been shown that oxidative processes occurring in KOH solutions can adjust the surface Fe/Ni atomic ratio to provide values in the range of 0.2–0.4. Under these conditions, the density of nickel redox sites (typically evaluated using the Ni^{3+}/Ni^{2+} redox capacity as an indicator) reaches a maximum, resulting in high OER activity.[19] Despite the potential of SS, the majority of OER studies employing SS electrodes have been performed using highly alkaline electrolytes (typically 0.1–5 M KOH; $M = mol\ dm^{-3}$). Systematic investigations of the oxidation characteristics and OER activities of SS anodes in the phosphate-buffered electrolytes discussed above have been scarce. Moreover, studies focusing on the interactions between SS and phosphate-buffered electrolytes as a means of assessing the stability of SS in such environments have been restricted to analyses of corrosion behavior.[20–22] Interestingly, recent studies have suggested that the use of mixed buffer electrolytes can have unexpected effects on the structure and stability of electrocatalysts.[23–26] As an example, Nishimoto *et al.* reported that interactions between phosphate ions and electrode surfaces containing nickel or copper promote the hydrogen evolution reaction over the pH range of 9–12.[26]

Based on this background, the aim of the present study was to systematically investigate the effects of the oxidation of SS in phosphate-buffered electrolytes on surface composition and OER activity. A further goal was to elucidate the manner in which the unique chemical environment of phosphate buffers affects the formation and composition of surface oxide films based on a comparison with KOH electrolytes. Finally, by establishing correlations between the electrode condition and OER activity, this work was intended to promote the development of highly active yet stable electrode materials.

Experimental section

Preparation of electrolytes

Ultrapure water (Milli-Q Reference A+, Millipore Co.) having a resistivity of 18.2 MΩ cm was used as the solvent for all electrolytes. Potassium hydroxide (KOH; FUJIFILM Wako Pure Chemical) and dipotassium hydrogen phosphate (K_2HPO_4; FUJIFILM Wako Pure Chemical, purity ≥99.0%) were used as solutes. The electrolytes employed in this study consisted of 0.2, 1 or 3 M K_2HPO_4 or 1 M KOH solutions. The pH of each K_2HPO_4 electrolyte was adjusted to approximately 11.5 by the addition of KOH. To avoid the effects of alkaline errors associated with the use of a glass electrode for pH measurements, the pH adjustments were carried out using the fixed, predetermined K_2HPO_4 : KOH molar ratio of 1 : 0.0364 in the case of the 1 M K_2HPO_4 and 3 : 0.0819 in the case of the 3 M K_2HPO_4 to give a pH of approximately 11.5. The ionic conductivity and viscosity values for these electrolytes are summarized in Table S1. Viscosity measurements were performed using an electromagnetic spinning viscometer (EMS-1000, KEM) while ionic conductivity data were acquired using a conductivity meter (ES-51, HORIBA).

Electrochemical measurements

Electrochemical measurements were performed using a potentio/galvanostat (SP-50 or SP-150, Bio-Logic Science Instruments) with a conventional three-electrode electrochemical cell. A bulk 304 stainless steel (304 SS) sheet (thickness: 0.2 mm; Nilaco) served as the working electrode while a Pt mesh (Nilaco) and an Ag/AgCl electrode in saturated KCl were used as the counter and reference electrodes, respectively. Prior to measurements, the 304 SS substrates were cleaned by immersion in Ace Clean 801E (Okuno Chemical Industries Co., Ltd) heated to 130 °C for more than 10 min to remove any organic contaminants, followed by thorough rinsing with water and drying. The native oxide layer of the metal was subsequently removed by immersion in Top-san (Okuno Chemical Industries Co., Ltd) at room temperature for approximately 1 min. After rinsing with water and drying, a circular area on the electrode with a diameter of 8 mm (geometric area: 0.50 cm^2) intended for contact with the electrolyte was defined using a sample holder (AE9-1, EC-FRONTIER), after which each electrode was used for electrochemical measurements. All such trials were conducted at room temperature and ambient pressure with a rotational rate of 500 rpm.

Sample characterization

Prior to observation, the surface of each sample was thoroughly rinsed with water and dried. Assessments using transmission electron microscopy (TEM; JEM-2100F, JEOL) were performed at an accelerating voltage of 200 kV. Elemental analysis was carried out using energy-dispersive X-ray spectroscopy (EDX; JED-2300T, JEOL). Cross-sectional TEM samples were prepared by embedding each oxidized sample in epoxy resin, followed by mechanical polishing to expose the cross section and thinning by ion milling. Gamma correction was applied to scanning transmission electron microscopy (STEM) images to enhance image contrast. Low-magnification surface observations were conducted using scanning electron microscopy (SEM; TM4000plus, HITACHI) at an accelerating voltage of 20 kV. X-ray photoelectron spectroscopy (XPS) data were obtained using a scanning XPS instrument (PHI VersaProbe 4, ULVAC-PHI) with monochromated Al Kα radiation (1486.6 eV) at a power level of 25 W with an accelerating voltage of 15 kV. The analysis area had a diameter of 100 μm. Unless otherwise noted, Ar sputter etching was not applied to the samples. All spectra were energy-calibrated using the C 1s peak of adventitious carbon at 284.8 eV as a reference. Thickness corrections based on the inelastic mean free path were not applied during compositional analyses.

Electrochemical quiescent crystal microbalance

In situ monitoring of the mass changes associated with electrochemical reactions was performed using a quartz crystal microbalance (QCM; QCM-922A, SEIKO EG&G). Changes in the resonance frequency of the QCM (Δf_m) were approximately converted to mass changes on the electrode surface (Δm) using the Sauerbrey equation. The relationship $\Delta m/\Delta f_m = -1.07$ ng Hz^{-1} was used in the case of the QCM crystals employed in this study. The frequency shifts observed during QCM analyses were determined both by the magnitude of Δm and by changes in the resistance of the resonator to motion. However, throughout the present electrochemical QCM (EQCM) measurements, the experimentally observed temporal variations in the resonance resistance were less than several ohms, indicating that the contribution of this effect to the frequency response was negligible. The EQCM experiments were conducted using a three-electrode cell connected to a potentiostat and all data were acquired at room temperature. The EQCM cell was configured with a 304 SS QCM electrode (QA-A9M-SUS304, electrode area: 0.196 cm^2, SEIKO EG&G) as the working electrode, a Pt mesh as the counter electrode, and an Ag/AgCl electrode in saturated KCl as the reference electrode. According to the manufacturer, the QCM electrode was fabricated by a sputter deposition process in which a 100 nm Ti adhesion layer was first deposited followed by a 300 nm 304 SS layer. The standard-finish quartz crystals used in this apparatus were polished with alumina (#4000) to achieve a roughness of approximately 0.6 μm and subsequently subjected to an etching treatment. The 304 SS layer had a nominal composition consisting primarily of Fe (66.5–74 wt%), Cr (18–20 wt%), and Ni (8–10.5 wt%), along with minor amounts of Mn (≤2 wt%) and Si (≤1 wt%).

Fig. S1 shows SEM images of the surface of a QCM-type SS electrode and of a bulk 304 SS sheet electrode, while Table S2 summarizes the surface atomic fractions obtained from EDX analyses. No significant differences in alloy composition were observed between the two electrodes and comparable time–potential curves exhibiting similar trends were obtained regardless of which electrode was used (Fig. S2).

Procedure for the oxidative treatment

Electrochemical oxidation of the 304 SS was performed following previously reported procedures,[19,27] using either 1 M K_2HPO_4 or 1 M KOH solutions as the electrolytes. This oxidative treatment consisted of two steps. In step (1), a constant-potential electrolysis cycle was applied, comprising polarization at 1.581 V *vs.* RHE for 10 min followed by polarization at 0.981 V *vs.* RHE for 5 min. This cycle was repeated twice. In step (2), a bidirectional potential sweep was performed twice over the potential range of 1.061–1.581 V *vs.* RHE at a scan rate of 5 mV s^{-1} to acquire cyclic voltammetry (CV) data. Potentials measured *versus* RHE were converted to the Ag/AgCl (sat. KCl) scale using the equation $E_{\mathrm{RHE}} = E_{\mathrm{Ag/AgCl(sat.)}} + 0.197 + 0.0591\ \mathrm{pH}$. This series of operations, consisting of steps (1) and (2), was programmed into the potentiostat and repeated 12 times in total. These conditions were selected based on the expectation that nickel-based active sites would be generated *via* repeated modulation of the potential between values higher than that required for Ni^{3+} formation and lower than that required for Ni^{2+} formation. Hereafter, the samples subjected to the above oxidative treatment using 1 M K_2HPO_4 or 1 M KOH are referred to as K_2HPO_4-treated and KOH-treated, respectively.

Evaluation of nickel redox capacity

The nickel redox capacity for each trial was determined by integrating the Ni^{3+}/Ni^{2+} reduction peak obtained from CV data recorded at a scan rate of 50 mV s^{-1}. This process employed data from the eleventh CV cycle because, by this point, the voltammograms had reached a quasi-steady state and exhibited reproducible shapes. Under alkaline conditions, the nickel species involved in the Ni^{3+}/Ni^{2+} redox couple are known to correlate strongly with OER activity.[28] Accordingly, in this study, the Ni^{3+}/Ni^{2+} redox capacity was used as an indicator of the number of nickel redox sites, assuming that both Ni^{3+} and Ni^{2+} contribute to catalytic activity.

Results and discussion

Potential-dependent oxidative reactions on SS electrodes in phosphate electrolytes

Subtle changes associated with the surface of a SS electrode in phosphate-buffered electrolytes were monitored by performing QCM trials under galvanostatic conditions. In these experiments, galvanostatic electrolysis was conducted at a current density of 10 μA cm^{-2} using a 304 SS electrode having an area of 0.196 cm^2 in a 1 M K_2HPO_4 solution while tracking the associated mass changes using the QCM (Fig. 1). During the initial stage of electrolysis, the electrode potential increased monotonically from approximately 0.2 to 0.8 V, accompanied by a decrease in the electrode mass. Subsequently, the potential became nearly constant at approximately 0.8 V while the rate of mass increase gradually diminished. A similar trend was observed when electrolysis was carried out at a higher current density of 100 μA cm^{-2} (Fig. S3). In addition, in the case that galvanostatic electrolysis was temporarily interrupted and then resumed at the same current density after a 5 min open-circuit period, the electrode potential immediately returned to approximately 0.8 V upon restarting the electrolysis (Fig. S4). These results indicate that, once the electrode surface reached a state corresponding to a potential of approximately 0.8 V, it retained this surface condition even after the interruption.

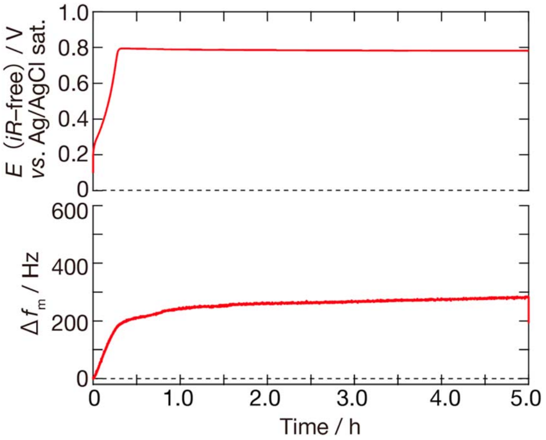

Fig. 1 EQCM plots obtained from a QCM-type 304 SS electrode at room temperature under a constant current of 10 μA cm^{-2} in 1 M K_2HPO_4 (pH11.5).

Upon resumption of galvanostatic electrolysis, the system rapidly returned to an electrochemical reaction state such that the reaction proceeded at a potential in the vicinity of 0.8 V.

The electrochemical processes occurring at the electrode surface at various electrode potentials were examined by carrying out potentiostatic electrolysis over 5 h at potentials of either 0.4 or 0.8 V while monitoring variations in mass with the QCM (Fig. S5). During electrolysis at 0.4 V, Δf_m was found to continually increase throughout the experiment, corresponding to a net decrease in the electrode surface mass. During electrolysis at 0.8 V, an initial mass decrease similar to that observed at 0.4 V was also evident during the early stage of the process. However, after approximately 2 h, the frequency shift instead began to decrease, indicating the onset of net mass accumulation at the electrode surface. These results suggest that, at 0.4 V, processes promoting the removal of surface species, such as the dissolution of surface metal components, were predominant. Conversely, at 0.8 V, the initially dominant dissolution process was gradually overtaken by the formation of an oxide film as electrolysis proceeded. Hence, it appears that distinct electrochemical reactions occurred, depending on the applied potential.

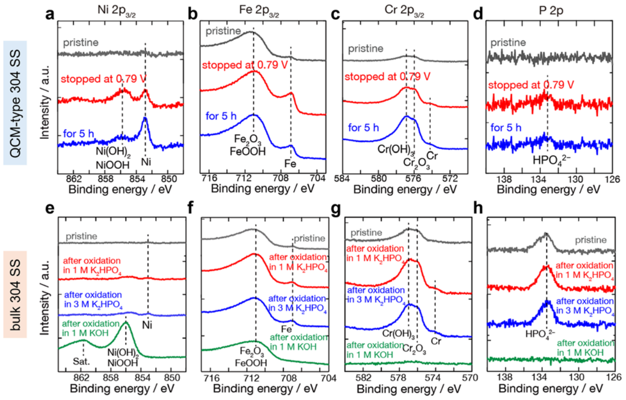

Fig. 2 Ni 2p, Fe 2p, Cr 2p, and P 2p XPS data acquired from (a–d) QCM-type 304 SS electrodes after galvanostatic electrolysis at 10 μA cm^{-2} in 1 M K_2HPO_4, during which electrolysis was stopped when the potential reached 0.79 V (red) or continued for 5 h under the same conditions (blue), and (e–h) bulk 304 SS sheet electrodes oxidized under previously reported conditions[19,27] in 1 M K_2HPO_4 (red), 3 M K_2HPO_4 (blue), or 1 M KOH (green). Gray lines represent data for a pristine 304 SS electrode.

The surface states associated with different electrochemical conditions were compared by carrying out galvanostatic electrolysis experiments at a current density of 10 μA cm^{-2}. These trials were used to fabricate two types of samples, either by stopping electrolysis when the electrode potential reached 0.79 V (corresponding to a total duration in the range of 10–30 min) or by continually performing electrolysis under the same conditions for a total duration of 5 h. These specimens were then evaluated using XPS (Fig. 2a–d). It should be noted that, in the case that monochromated Al Kα radiation was used as the XPS excitation source, the Fe 2p signals overlapped with the Ni LMM Auger peaks, requiring careful interpretation of the spectra. According to previous reports, samples subjected to oxidation in KOH solutions exhibit a marked decrease in metallic Ni accompanied by a pronounced increase in peaks attributable to $Ni(OH)_2$/NiOOH, indicating the formation of a nickel-dominated oxyhydroxide surface layer.[17,19,29,30] In addition, iron has been detected in the form of Fe_2O_3 or FeOOH and has been shown to be incorporated into the surface layer *via* uptake from the electrolyte.[31,32] That is, iron is thought to undergo oxidative dissolution from the stainless steel followed by redeposition. In contrast, the surface concentrations of other alloying elements in the 304 SS, such as chromium, are reported to decrease significantly during the oxidation process, ultimately leading to a surface enriched in Ni/Fe oxides.[31] Interestingly, the results obtained in the present phosphate-buffered electrolyte differed markedly from those previously observed in trials using KOH as the electrolyte. Specifically, the growth and deposition of nickel and iron oxides was suppressed while stable Cr_2O_3 and/or $Cr(OH)_3$ deposits were formed on the electrode surface. Furthermore, XPS analyses indicated there were no significant differences in the surface compositions of the two specimens prepared with different electrolysis durations (Fig. 2a–d). Therefore, the mass decrease observed during the potentiostatic experiment at approximately 0.8 V is attributed to the transpassive dissolution of metal ions, as has been observed in prior work.[20] It should be noted that this process did not involve substantial changes in the surface state of the film. That is, the electrode surface state was largely maintained at approximately 0.8 V and even under conditions that would be expected to promote transpassive dissolution. The anodic reaction occurring at the electrode surface therefore appears to have primarily comprised the OER rather than metal dissolution.

The effect of phosphate concentration on the oxidation of SS electrodes

The effect of the phosphate concentration was examined by carrying out galvanostatic electrolysis at a current density of 10 μA cm^{-2} in 0.2 or 3 M K_2HPO_4 while evaluating the associated mass by QCM (Fig. S6 and S7). Although qualitatively similar behavior was observed at both concentrations, the oxidation potential reached approximately 0.8 V within a shorter time at the lower phosphate concentration of 0.2 M. Furthermore, the mass change observed after reaching this potential was lower at the lower phosphate concentration. Previous studies have suggested that phosphate may be adsorbed on the electrode.[33,34] However, the effect of phosphate concentration observed in the present study cannot be fully explained based on phosphate adsorption as the dominant process. In general, if surface adsorption of a chemical species by either physisorption or chemisorption is dominant, increasing the solution concentration or the activity of that species should promote adsorption and thus lead to a net gain in mass. In contrast, in the present case, the opposite effect was evident. Moreover, if the adsorption of phosphate was promoted at higher concentrations, metal dissolution would be expected to be suppressed *via* a protective effect, but this was not observed. Instead, higher phosphate concentrations were found to promote the loss of metal species from the 304 SS. This enhanced dissolution is attributed to the formation of soluble phosphate complexes such as $NiHPO_4$(aq) and $FeHPO_4$(aq). Experimental observations consistent with this interpretation[35] as well as reports concerning the formation of soluble phosphate complexes[36,37] have been previously published, in good agreement with the results obtained in this study.

Surface changes of SS electrodes under more severe oxidizing conditions

The previous section examined the oxidation reactions occurring at each potential and the corresponding surface states of the SS electrodes, while demonstrating that the surface states formed in phosphate electrolytes differed from those in KOH solutions. The SS surface oxidation discussed above was conducted under galvanostatic conditions at 10 or 100 μA cm^{-2}, representing relatively mild oxidation conditions. Following this, oxidation trials were performed using a different protocol based on previously reported procedures, to determine if more severe oxidation conditions also produced surface changes different from those observed in KOH.[19,27] These procedures are described in the Experimental section. This protocol was designed based on the assumption that a nickel-rich active layer could be generated through repeated modulation between higher and lower potentials (Fig. S8). The XPS results obtained after this oxidative treatment are shown in Fig. 2e–h. These data show no significant variations compared with the sample prepared under galvanostatic conditions (10 μA cm^{-2}) in a phosphate electrolyte, during which electrolysis was stopped when the potential reached 0.79 V (Fig. 2a–d). The Fe/Ni atomic ratio calculated from the surface atomic fractions (in at%) determined by XPS was 72.3 for the pristine 304 SS electrode without oxidative treatment. After immersion in KOH, this ratio decreased to 0.646 whereas the electrode immersed in the phosphate electrolyte exhibited a significantly higher Fe/Ni ratio of 13.5. Furthermore, in agreement with previous reports,[17,19,29] the XPS spectra of the KOH-treated samples did not contain peaks corresponding to zero-valent Ni, Fe, or Cr. In contrast, these metallic peaks were observed in the case of the specimens processed in the K_2HPO_4 electrolytes. This difference is ascribed to the thinner oxide film formed in the K_2HPO_4 solutions, which was less than the typical XPS analysis depth of approximately 5–10 nm, such that the data also reflected the underlying metallic substrate.

Cross-sectional STEM observations were performed to further examine the surface films formed on these samples (Fig. 3). In the case of the sample treated in the KOH solution, a film having a thickness of approximately 20 nm was observed on top of a chromium oxide layer with a thickness of approximately 3 nm associated with the SS. Nanobeam electron diffraction analyses of this film produced diffraction patterns corresponding to NiO. This phase is thought to have resulted from the presence of NiOOH or $Ni(OH)_2$, which had been identified as the main components of the surface film by XPS, during specimen preparation as a result of heating and/or ion

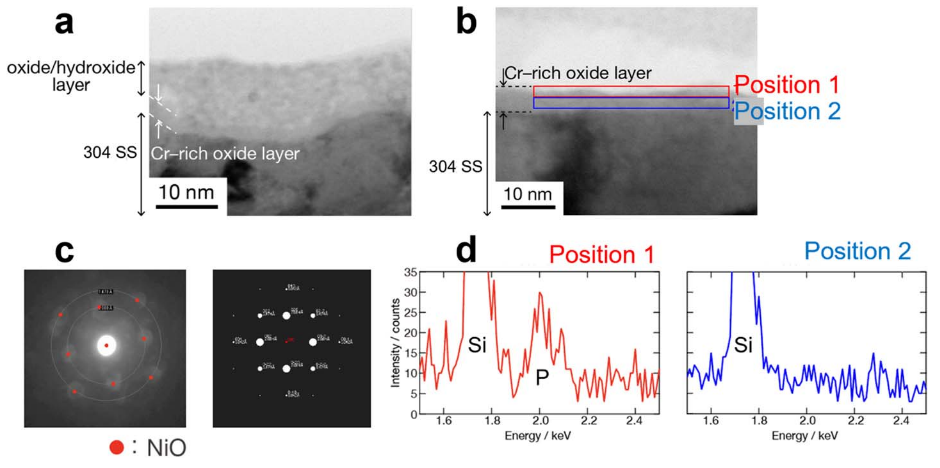

Fig. 3 Cross-sectional STEM images of 304 SS sheets following processing in (a) 1 M KOH and (b) 1 M K_2HPO_4 (pH11.5). (c) Nanobeam electron diffraction pattern produced by the oxide film formed on the KOH sample (left) together with the simulated diffraction pattern for NiO along the [100] zone axis (right). (d) EDX spectra showing the P signal acquired from the K_2HPO_4 specimen at positions 1 and 2 as indicated in (b).

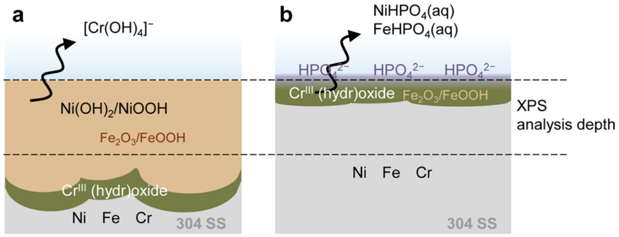

Fig. 4 Diagrams showing oxide film formation on 304 SS electrodes in the (a) KOH and (b) K_2HPO_4 electrolytes (pH11.5). In the former, anodic oxidation results in the growth of nickel and iron oxyhydroxide layers with the concurrent depletion of chromium, yielding a surface with nickel redox sites. In the latter, the selective dissolution of nickel and iron combined with retention of insoluble iron and chromium compounds leads to the formation of a thin chromium-rich passivation layer.

beam irradiation. In contrast, the K_2HPO_4-treated specimen surface showed only a chromium oxide layer with a thickness of approximately 3 nm with no additional film components. EDX analyses of the outermost surface region and within the chromium oxide layer found the presence of P solely within approximately 2 nm of the outermost surface (Fig. 3d and f). This finding indicates that P was partially incorporated into the surface film and localized only in the near-surface region of the electrode. In contrast to the electrode processed in the KOH solution, a strong nickel signal was not obtained from the surface film (Fig. S9). Based on these XPS and TEM results, it is concluded that even severe oxidative conditions intended to promote the formation of a nickel-rich oxyhydroxide active layer did not generate such a surface layer in the phosphate-buffered electrolytes, in contrast to the KOH electrolytes. Instead, an extremely thin surface film was formed, consisting of a chromium oxide layer derived from the SS itself as the base and a phosphorus-containing region localized near the outermost surface. Schematic illustrations of the surface films formed in KOH and phosphate-buffered electrolytes are provided in Fig. 4. These findings demonstrate that the formation of surface films on the SS electrodes was largely determined by the electrolyte composition as opposed to the oxidative conditions.

OER activity of SS electrodes after surface treatment in phosphate electrolytes

Anodic polarization trials were carried out in phosphate-buffered electrolytes to drive the OER, as a means of evaluating the activity of the SS electrodes in this medium. The potentials required to reach current densities of 5 and 10 mA cm^{-2} were compared with those for untreated (pristine) electrodes (Fig. 5a). Regardless of whether the oxidative treatment was applied, the potentials required to reach both current densities were nearly identical, indicating that oxidative treatment in phosphate electrolytes had no pronounced effect on OER activity.

This result can be explained by the fact that, unlike the case of KOH-treated SS electrodes, the surface film formed in phosphate electrolytes reduced the exposure of redox-active nickel sites, thereby preventing enhancement of the OER activity. Studies of Ni–Fe-based electrodes under alkaline conditions have shown that the Ni^{3+}/Ni^{2+} redox couple is closely associated with OER activity.[28] Consistent with this understanding, the samples processed in phosphate electrolytes in this work produced weaker $Ni(OH)_2/NiOOH$ peaks in XPS spectra compared with the spectra of specimens immersed in KOH solutions (Fig. 2a and e). In agreement with these observations, the nickel redox capacity of a sample processed in a K_2HPO_4 solution, as shown in Fig. 5b, was 0.107 mC cm^{-2}. This value was significantly less than that determined for a KOH-treated sample (0.399 C cm^{-2}). It is evident that an oxidative treatment in a phosphate electrolyte inhibited the formation of nickel redox sites, thereby limiting enhancement of the OER activity.

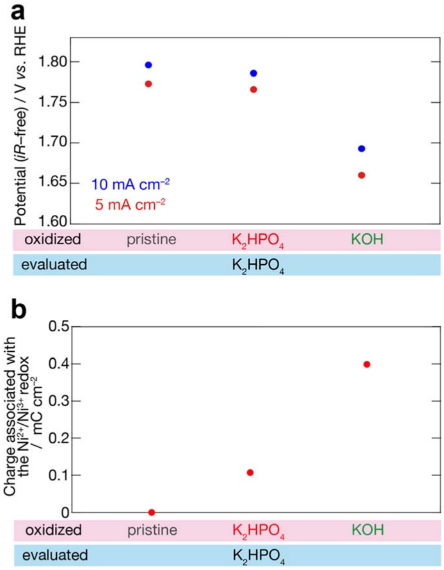

Fig. 5 (a) *iR*-free potentials obtained at current densities of 5 and 10 mA cm^{-2} and (b) charge capacity values associated with the Ni^{3+}/Ni^{2+} redox couple for bulk 304 SS sheet electrodes as determined from the cathodic CV peaks during the eleventh cycle. Electrodes were either pristine or oxidized in 1 M K_2HPO_4 or 1 M KOH, after which OER activities were evaluated in 1 M K_2HPO_4.

Mechanistic insight into oxide film formation in phosphate electrolytes

The results described thus far indicate that oxidative treatment in phosphate electrolytes had a minimal effect on the formation of electrochemically redox-active nickel sites. Consequently, no significant effect of this treatment on the OER activity of the electrodes was observed (Fig. 3a). Metallic Ni, Fe and Cr can all be oxidized on a thermodynamic basis within the potential range of 0–0.8 V *vs.* Ag/AgCl (sat.). Therefore, the observed mass changes are attributed to the reconstruction of oxide-dominated surface films and/or the dissolution of metal components. The effects of phosphate electrolytes have frequently been discussed primarily in terms of the blocking of active sites based on the adsorption of phosphate anions on the electrode surface.[33,34] If such adsorption were the dominant process, an increase in electrode mass would be expected. However, the EQCM data in this work show that the electrode mass instead decreased with increasing phosphate concentration (Fig. S6), such that an adsorption-based model is insufficient.

On this basis, an alternative mechanism for surface oxide film formation in phosphate electrolytes is proposed. This mechanism results in lessened nickel redox capacity (Fig. 4). In this process, the immersion of 304 SS in a phosphate electrolyte induces selective dissolution of nickel and iron from the electrode surface as soluble complexes such as $NiHPO_4$(aq) and $FeHPO_4$(aq) under open-circuit conditions. In this scenario, dissolved oxygen can act as an oxidant or simultaneous anodic oxidation can occur as the potential is swept to oxidative values.[36,37] Dissolved iron can partially reattach to the surface as oxides or hydroxides, which is consistent with the greater proportion of iron rather than nickel-based components observed during the XPS analyses. A small amount of the chromium oxide film can also dissolve on a thermodynamic basis in the form of hydrolysis products such as $Cr(OH)_3$. Even so, Cr(III) is sparingly soluble under neutral to mildly alkaline conditions and, unlike nickel and iron, does not form phosphate complexes (or at least none have been reported). As a result, solid $Cr(OH)_3$ remains on the surface or reattaches from solution.[38] During the CV trials and surface oxidation experiments, the transient dissolution and reprecipitation of surface chromium oxides occur repeatedly, thereby maintaining or forming a thin chromium-rich layer. Consequently, the electrochemically active nickel redox sites originally present on the outermost surface are effectively reduced in number and become shielded from participating in surface reactions.

In contrast, in KOH electrolytes, nickel and iron are not dissolved *via* phosphate complex formation, and oxidative treatment instead leads to an increase in $Ni(OH)_2$/NiOOH.[17,19,29,30] In addition, Cr(III) is readily solubilized in strongly alkaline KOH solutions in the form of hydroxo complexes such as $[Cr(OH)_4]^-$. Under oxidative potentials, these complexes are stabilized in solution as Cr(VI) ions. Consequently, chromium is less likely to be immobilized on the surface and its dissolution is promoted. Evidence for this mechanism was provided by the present STEM-EDS observations (Fig. 3 and S9) and XPS results (Fig. 2e–h).

Both the XPS and cross-sectional STEM-EDX analyses indicated localization of P near the surfaces of samples following oxidation in the phosphate electrolytes (Fig. 2 and 3). This observation suggests that phosphate species were selectively enriched at the metal–electrolyte interface, thereby stabilizing the surface films. This behavior is reminiscent of well-established electropolishing models, in which interactions between metal ions and phosphate species in phosphate-based electrolytes lead to the formation of a viscous phosphate-rich layer near the metal surface.[39–41]

Stabilization of nickel redox sites by KOH pretreatment

Given that the formation of nickel redox sites is evidently suppressed in phosphate electrolytes, it could be possible to preform these redox sites *via* an oxidative treatment in a KOH solution, with the subsequent transfer of the electrode to a phosphate electrolyte for use in an OER system. If the Ni^{3+}/Ni^{2+} species generated during the oxidative treatment in the KOH electrolyte are retained after transfer to the phosphate electrolyte, such electrodes could potentially function as stable and highly active OER catalysts. Accordingly, the OER potential at a current density of 10 mA cm^{-2} was evaluated in a K_2HPO_4 electrolyte using KOH-treated electrodes prepared separately. As expected, the OER proceeded at a lower overpotential (1.692 V *vs.* RHE) compared with the value observed using an electrode oxidatively treated in K_2HPO_4 (1.786 V *vs.* RHE), demonstrating an enhancement in OER activity (Fig. 5a).

After using CV to evaluate the nickel redox capacity (which served as an indicator of the number of redox-active sites) in K_2HPO_4 at a scan rate of 50 mV s^{-1} over a potential range of 0.4–0.8 V *vs.* Ag/AgCl (sat.), XPS analyses of the electrode surfaces were carried out. The results confirmed that, even after electrochemical evaluation in K_2HPO_4, there were no substantial differences in surface composition or spectral features compared with fresh KOH-treated surfaces (Fig. S10). Thus, processing in K_2HPO_4 electrolytes and subsequent electrochemical trials produced chemical states of nickel, iron, and chromium at the electrode surfaces essentially equivalent to those resulting from the oxidative treatment in KOH, at least over the depth of 5 to 10 nm that was assessed. However, a clear decrease in the nickel redox capacity was observed upon transfer to the K_2HPO_4 electrolytes. The original value of 0.603 mC cm^{-2} in a KOH solution was reduced to 0.399 mC cm^{-2} in 1 M K_2HPO_4 and further to 0.156 mC cm^{-2} in 3 M K_2HPO_4 (Fig. S11).

Deactivation of redox-active nickel sites in phosphate electrolytes

The overall shapes of cyclic voltammograms were preserved even after repeated cycling in KOH electrolytes, and the nickel redox capacity was also stable (Fig. S12). In contrast, when an electrode was moved from a KOH solution to a phosphate electrolyte and subjected to repeated CV cycles, the redox peaks gradually diminished with cycling. Concurrently, a gradual increase in the OER overpotential was also observed. Upon further CV cycling in the K_2HPO_4 electrolyte, the redox peak corresponding to the Ni^{3+}/Ni^{2+} couple completely disappeared after 250 cycles (corresponding to an experimental duration of approximately 1 h) (Fig. 6a). XPS assessments of the electrode surface after 250 CV cycles showed the emergence of a new peak in the P 2p region attributable to HPO_4^{2-}. No significant changes were detected in the surface proportions or chemical states of the other elements (Fig. S13).

The nickel redox capacity was reduced but no noticeable changes occurred in the amounts or chemical states of elements other than P (according to the XPS analysis), because of the different probing depths associated with the electrochemical redox process and the XPS assessment. Specifically, the XPS returned information to a depth of several tens of nanometers. In contrast, the nickel redox capacity was associated solely with several of the outermost atomic layers on the electrode surface.

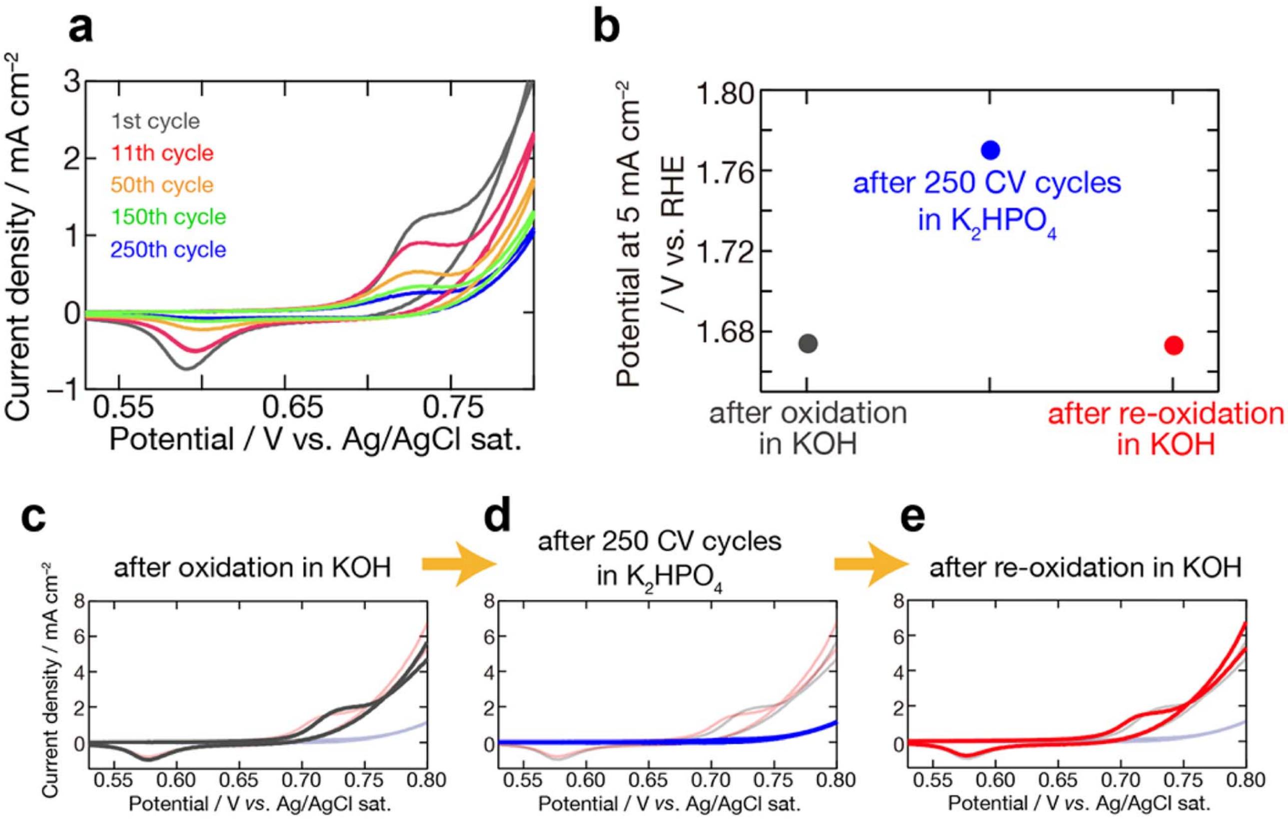

Fig. 6 (a) Representative CV data acquired to evaluate the Ni^{3+}/Ni^{2+} redox capacity of a 304 SS electrode in a phosphate electrolyte at a scan rate of 50 mV s^{-1} at room temperature. (b) Comparison of the potentials at a current density of 5 mA cm^{-2} for the corresponding electrodes. CVs obtained (c) from the first cycle in a 1 M K_2HPO_4 electrolyte (pH11.5) after KOH pretreatment, (d) from the 250th cycle in a 1 M K_2HPO_4 electrolyte, and (e) from the first cycle in a 1 M K_2HPO_4 electrolyte after subsequent re-oxidation in 1 M KOH.

This is evident from the small magnitude of the observed redox charges, which were at most approximately 0.4 mC cm^{-2} (Fig. 3a), whereas a single monolayer would be expected to provide a charge of approximately 0.16 mC cm^{-2}. Therefore, even if the surface region responsible for the redox activity was completely lost, the XPS data would not necessarily indicate any changes as long as the underlying region, extending several nanometers into the bulk, remained chemically and compositionally unchanged.

All the experiments described above were conducted at room temperature. To examine the effect of temperature, additional CV trials were performed using an electrode previously immersed in a KOH solution, employing 250 cycles in a K_2HPO_4 electrolyte at 70 °C. The results were compared with those obtained at ambient temperature (Fig. S14). At elevated temperatures, the nickel redox peak disappeared after approximately 75 cycles, indicating that the redox capacity decayed more rapidly. Increasing the concentration of the phosphate electrolyte led to an even faster decrease in capacity, accompanied by a corresponding increase in the OER overpotential (Fig. S15 and S16). Similar results were obtained after setting the anodic switching potential to a more cathodic value (Fig. S17). In addition, when the KOH-treated electrodes were simply immersed in phosphate electrolytes under open-circuit conditions for a defined period prior to acquiring CV data, the nickel redox capacity was found to decrease. The extent of this decrease increased with longer immersion times (Fig. S18). These results indicate that the loss of capacity proceeded even at the open-circuit potential and did not require repeated CV cycling.

Mechanistic insights into the deactivation of nickel redox sites in phosphate electrolytes

When surface films pre-activated by immersion in KOH solutions were transferred to a phosphate electrolyte, the nickel redox capacity was decreased followed by a gradual and irreversible loss of activity (Fig. 6a). These findings suggest that, even if electrochemically redox-active nickel-based sites were initially present on the KOH-treated electrode, these sites were continually removed from the outermost surface upon immersion in a phosphate electrolyte. This loss of nickel redox sites appeared to arise simply from immersion of the KOH-treated electrode in a phosphate electrolyte, which caused nickel and iron on the electrode surface to form soluble complexes such as $NiHPO_4(aq)$ and $FeHPO_4(aq)$ (Fig. 7a).[36,37] The accelerated decrease in the nickel redox capacity with increasing immersion solution temperature, phosphate concentration or immersion time indicate that all three variables affected the dissolution of nickel and iron as well as the accumulation of phosphate ions on the electrode surface. In particular, the much greater loss of nickel redox capacity at higher temperatures and phosphate concentrations cannot be adequately explained by simple

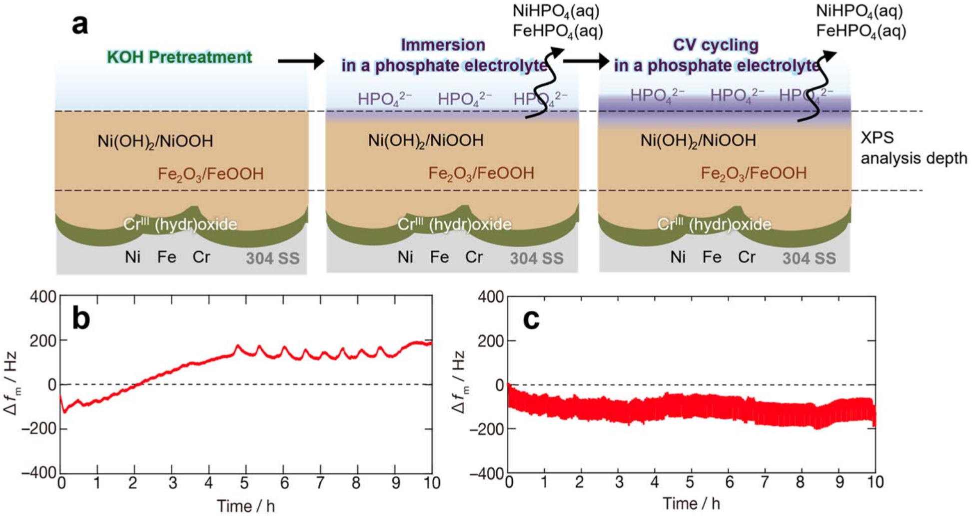

Fig. 7 (a) A schematic illustration of the surface evolution of a 304 SS electrode pretreated in KOH and subsequently transferred to a phosphate-based electrolyte (pH11.5). (b and c) EQCM frequency shift (Δf_m) responses of a KOH-pretreated 304 SS sheet electrode during (b) immersion at the open-circuit potential for 10 h in 1 M K_2HPO_4 and (c) CV in 1 M K_2HPO_4. The CV data were obtained over the potential range of 0.5–0.8 V at a scan rate of 50 mV s^{-1}.

obscuration of the surface based on phosphate adsorption. Instead, it appears that dissolution processes involving nickel and iron played a more dominant role. Under the present conditions, the surface films were extremely thin and thus each film represented only a very small fraction of the specimen volume that was assessed. In addition, because nickel and iron had already dissolved from the near-surface region, even surface-sensitive techniques such as XPS were unable to detect further decreases in these metals, explaining the absence of pronounced changes in the XPS spectra.

In the case that the nickel redox capacity of a KOH-pretreated electrode was evaluated following electrolysis in 1 M K_2HPO_4 at a current density of 50 mA cm^{-2} for 5 h, redox peaks were not observed (Fig. S19). This result suggests that, under high current density conditions, an electrode surface depleted of nickel and iron (such as that illustrated in Fig. 7a) is rapidly generated early in the OER process. Because only minor changes in electrode potential were observed during electrolysis, it appears that the electrode surface quickly transitioned to a steady state early in the reaction.

The mechanism responsible for the loss of nickel-based active sites in conjunction with metal dissolution and surface film formation was further examined by using the EQCM technique to monitor the mass of a KOH-treated electrode during immersion in a phosphate electrolyte at the open-circuit potential or during CV trials over the potential range of 0.5–0.8 V (Fig. 7b and c). In the former case, a frequency increase, Δf_m, of approximately 150 Hz was observed, equivalent to a mass decrease of approximately 160 ng. In contrast, during the latter experiments, a decrease on the order of 100 Hz was evident, corresponding to a mass increase of approximately 107 ng. If the mass decrease of 160 ng observed during open-circuit immersion is attributed to the dissolution of nickel and iron, the amount of dissolved metal would equate to approximately 8×10^{15} atoms cm^{-2}. Considering that the atomic surface density of a face centered cubic metal is on the order of 10^{15} atoms cm^{-2}, this dissolution corresponds to at most only a few monolayers. However, if the mass increase of 107 ng observed during CV trials is attributed to the adsorption of phosphate at the electrode–electrolyte interface, the surface density of phosphate would be approximately 5–6 nmol cm^{-2}. Taking into account the size of the hydrogen phosphate ion (HPO_4^{2-}), this value corresponds to a surface density equivalent to several monolayers. It is well known that interactions between metal ions and phosphate ions in an electrolyte produce a hydrated, viscous phosphate-rich layer near the metal surface. Therefore, the mass increase detected by EQCM is thought to result from adsorbed phosphate ions as well as strongly bound water molecules and viscous coupling effects. Taken together, these results provide evidence that metal dissolution proceeded even under non-electrochemical conditions in the phosphate electrolytes with dissolved oxygen functioning as an oxidant. In the case of experiments involving potential sweeps, phosphate ions were selectively accumulated at the electrode–electrolyte interface, thereby stabilizing the surface film that was formed.

Reactivation of nickel redox sites in KOH electrolytes

In the phosphate electrolytes, a stable surface layer was formed *via* the selective localization of phosphate ions at the electrode–electrolyte interface. In contrast, in the KOH electrolytes, OH^- ions preferentially coordinated to the metal surface, rendering the phosphate-derived surface overlayer thermodynamically unstable. Moreover, both nickel and iron were thermodynamically stable as hydroxides or oxyhydroxides in the KOH solutions.[42] Hence, the oxidative dissolution of these metals *via* the formation of soluble complexes, as occurred in the phosphate electrolytes, was less likely to proceed. Accordingly, immersing electrodes on which redox sites had been depleted by contact with phosphate electrolytes in a KOH electrolyte would be expected to lead to the reconstruction or removal of the phosphate-derived surface overlayer and the reactivation of nickel-based electrochemically redox-active sites. To verify this hypothesis, electrodes on which the redox sites had been depleted were subjected again to oxidative treatment in KOH after the procedure described in the Experimental section. Following this process, redox peaks corresponding to the Ni^{3+}/Ni^{2+} couple clearly reappeared (Fig. 6c–e). The redox capacity at this stage was comparable to that of the electrode immediately after immersion in a KOH solution. XPS analyses established that the P-based species detected on the surface after 250 CV cycles in a K_2HPO_4 electrolyte were no longer observed after a subsequent KOH treatment. At the same time, no significant changes in the surface states of other elements, such as nickel, iron or chromium, were evident for any of the samples. Notably, P was the only element that became undetectable on the reactivated electrode surface (Fig. S13). These results demonstrate that the surface overlayer formed in phosphate electrolytes was removed or reconstructed by the KOH treatment, leading to the re-exposure of surface nickel-based active sites and the consequent recovery of both nickel redox capacity and OER activity.

Conclusions

The oxidation of 304 SS electrodes in phosphate-buffered electrolytes and associated changes in surface states and OER activity were systematically investigated by combining EQCM, XPS, cross-sectional STEM-EDX, and electrochemical techniques. The results clearly demonstrate that the surfaces formed on SS electrodes in phosphate electrolytes were intrinsically different from the nickel-dominated oxyhydroxide layers formed in KOH electrolytes. In phosphate electrolytes, nickel and iron were preferentially dissolved *via* the formation of soluble phosphate complexes. However, Cr(III) species are only sparingly soluble under neutral to mildly alkaline conditions and are known not to form phosphate complexes (at least none have been reported). For these reasons, chromium remained on the electrode surfaces or was re-fixed as $Cr(OH)_3$. Consequently, an ultrathin chromium-rich surface film was formed and phosphate ions were localized at the electrode–electrolyte interface. This surface structure was maintained regardless of the severity of the oxidative conditions. This surface overlayer effectively decreased the number of available nickel-based electrochemically redox-active sites within the outermost few monolayers, leading to an irreversible decrease in the nickel redox capacity. Such depletion of redox-active sites may also occur when using electrodes with nickel-based surfaces, such as nickel foam or Ni-coated 304 SS. In contrast, in KOH electrolytes, a nickel-dominated active layer was readily formed and maintained. As such, even electrodes that had been deactivated in phosphate electrolytes fully recovered both the original nickel redox capacity and OER activity upon immersion in KOH. While the effects of phosphate electrolytes have typically been discussed primarily in terms of surface adsorption effects, the present results demonstrate that metal dissolution and surface reconstruction mediated by complex formation play a dominant role in governing electrode activity. These findings therefore challenge the conventional understanding of phosphate-based electrolytes and highlight the critical importance of considering electrolyte-induced complexation and surface reorganization in the design and evaluation of OER electrocatalysts.

The present study focused on the high-potential region within which the OER proceeds and phosphate ions promote the dissolution of nickel and iron through complex formation. However, in the case that the electrode potential is set to a cathodic value, dissolved metal species may redeposit or be re-fixed at the surface, giving rise to dynamic surface reconstruction that depends on the potential history. The various unusual surface behaviors that have been observed in phosphate-containing electrolytes may therefore originate from such dissolution–redeposition processes mediated by phosphate complexation.

These results demonstrate that there are intrinsic limitations to the application of phosphate-based electrolytes to catalytic systems whose activity relies on nickel redox processes. At the same time, the insights obtained in this study extend beyond phenomena specific to phosphate electrolytes and clearly highlight the critical importance of electrolyte design and interfacial chemistry. These insights pertain to a broad range of catalytic systems in which the reaction activity depends on redox-active transition metal sites. In particular, it is important to consider that complex formation induced by buffers, additives, or even contaminants in the electrolyte can trigger the selective dissolution and redeposition of transition metals providing active sites, leading to the depletion of catalytic active sites. This highlights that electrolyte composition and impurities can significantly influence the chemical state and activity of the electrode surface. Nevertheless, as shown in this study, these sites can be partially maintained or restored even in such electrolytes through appropriate strategies, such as pre-activation in KOH and control of the electrolyte composition and electrode potential. Therefore, an integrated approach that simultaneously controls electrolyte design, pretreatment conditions, and interfacial chemistry is a fundamental requirement for achieving both high performance and long-term stability of water electrolysis electrodes under neutral to mildly alkaline conditions.

Author contributions

K. N. conceived and designed the study and wrote the manuscript. S. H. performed the experiments and analyzed the data. K. M. supervised the research and provided critical advice and revisions to the manuscript. All authors discussed the results and approved the final version of the manuscript.

Conflicts of interest

The authors declare no competing financial interest.

Data availability

The data supporting the findings of this study are available within the article and its supplementary information (SI).

Supplementary information is available. See DOI: https://doi.org/10.1039/d6ta02355j.

Acknowledgements

This work was financially supported by JST GteX Program (grant no. JPMJGX23H2), JST-Mirai Program (grant no. JPMJMI21EA), ENEOS Tonengeneral Research/Development Encouragement & Scholarship Foundation, and Kansai Research Foundation for Technology Promotion (grant no. 2023R003). The authors thank Prof. Kazuhiro Fukami (Kyoto University) and Dr Shoichi Matsuda (National Institute for Materials Science) for their fruitful discussions at the initial stage of this study. The authors acknowledge the use of shared experimental facilities of the Department of Materials Science and Engineering, Kyoto University. The authors also thank Mr Kenji Kazumi (Kyoto University) for his technical assistance.

References

1 M. Chatenet, B. G. Pollet, D. R. Dekel, F. Dionigi, J. Deseure, P. Millet, R. D. Braatz, M. Z. Bazant, M. Eikerling, I. Staffell, P. Balcombe, Y. Shao-Horn and H. Schäfer, *Chem. Soc. Rev.*, 2022, **51**, 4583–4762.

2 S. Anantharaj, S. R. Ede, K. Sakthikumar, K. Karthick, S. Mishra and S. Kundu, *ACS Catal.*, 2016, **6**, 8069–8097.

3 M. El-Shafie, *Res. Eng.*, 2023, **20**, 101426.

4 A. Franco and C. Giovannini, *Sustainability*, 2023, **15**, 16917.

5 D. Li, E. J. Park, W. Zhu, Q. Shi, Y. Zhou, H. Tian, Y. Lin, A. Serov, B. Zulevi, E. D. Baca, C. Fujimoto, H. T. Chung and Y. S. Kim, *Nat. Energy*, 2020, **5**, 378–385.

6 D. Henkensmeier, W.-C. Cho, P. Jannasch, J. Stojadinovic, Q. Li, D. Aili and J. O. Jensen, *Chem. Rev.*, 2024, **124**, 6393–6443.

7 H. Tüysüz, *Acc. Chem. Res.*, 2024, **57**, 558–567.

8 T. Nishimoto, T. Shinagawa, T. Naito and K. Takanabe, *ChemSusChem*, 2021, **14**, 1554–1564.

9 T. Nishimoto, T. Shinagawa, T. Naito and K. Takanabe, *J. Catal.*, 2020, **391**, 435–445.

10 J. Jin, K. Walczak, M. R. Singh, C. Karp, N. S. Lewis and C. Xiang, *Energy Environ. Sci.*, 2014, **7**, 3371–3380.

11 T. Shinagawa, M. T. Ng and K. Takanabe, *ChemSusChem*, 2017, **10**, 4155–4162.

12 T. Shinagawa and K. Takanabe, *J. Phys. Chem. C*, 2016, **120**, 1785–1794.

13 K. Obata, L. Stegenburga and K. Takanabe, *J. Phys. Chem. C*, 2019, **123**, 21554–21563.

14 M. Auinger, I. Katsounaros, J. C. Meier, S. O. Klemm, P. U. Biedermann, A. A. Topalov, M. Rohwerder and K. J. J. Mayrhofer, *Phys. Chem. Chem. Phys.*, 2011, **13**, 16384–16394.

15 W. Sheng, Z. Zhuang, M. Gao, J. Zheng, J. G. Chen and Y. Yan, *Nat. Commun.*, 2015, **6**, 5848.

16 L. De Silva Muñoz, A. Bergel, D. Féron and R. Basséguy, *Int. J. Hydrogen Energy*, 2010, **35**, 8561–8568.

17 N. Todoroki and T. Wadayama, *ACS Appl. Mater. Interfaces*, 2019, **11**, 44161–44169.

18 N. Todoroki and T. Wadayama, *Mater. Trans.*, 2023, **64**, MT–MH2022002.

19 L. Magnier, G. Cossard, V. Martin, C. Pascal, V. Roche, E. Sibert, I. Shchedrina, R. Bousquet, V. Parry and M. Chatenet, *Nat. Mater.*, 2024, **23**, 252–261.

20 M. Kadowaki, T. Moronaga, A. Nakamura, Y. Murase, T. Hashimoto, H. Katayama, K. Takanabe and Y. Tsutsumi, *J. Phys. Chem. C*, 2025, **129**, 15939–15948.

21 M. Lakatos-Varsányi, F. Falkenberg and I. Olefjord, *Electrochim. Acta*, 1998, **43**, 187–197.

22 C. Pan, Y. Song, W. Jin, Z. Qin, S. Song, W. Hu and D.-H. Xia, *Trans. Tianjin Univ.*, 2020, **26**, 135–141.

23 H. Komiya, K. Obata, M. Wada, T. Nishimoto and K. Takanabe, *ACS Sustain. Chem. Eng.*, 2023, **11**, 12614–12622.

24 H. Komiya, K. Obata, T. Honma and K. Takanabe, *J. Mater. Chem. A*, 2024, **12**, 3513–3522.

25 G. K. Gebremariam, K. Siraj and I. A. Pašti, *Catalysts*, 2025, **15**, 835.

26 T. Nishimoto, K. Obata, H. Komiya, T. Naito, K. Harada, M. Yoshida and K. Takanabe, *ACS Catal.*, 2023, **13**, 14725–14736.

27 F. Moureaux, P. Stevens, G. Toussaint and M. Chatenet, *Appl. Catal., B*, 2019, **258**, 117963.

28 L. Trotochaud, S. L. Young, J. K. Ranney and S. W. Boettcher, *J. Am. Chem. Soc.*, 2014, **136**, 6744–6753.

29 N. Todoroki, A. Shinomiya and T. Wadayama, *Electrocatalysis*, 2022, **13**, 116–125.

30 Y. Deo, N. Thissen, V. Seidl, J. Gallenberger, J. Hoffmann, J. P. Hofmann, B. J. M. Etzold and A. K. Mechler, *Electrochem. Sci. Adv.*, 2025, **5**, 1–11.

31 Y. Zuo, V. Mastronardi, A. Gamberini, M. I. Zappia, T. Le, M. Prato, S. Dante, S. Bellani and L. Manna, *Adv. Mater.*, 2024, **36**, 2312071.

32 D. Y. Chung, P. P. Lopes, P. Farinazzo Bergamo Dias Martins, H. He, T. Kawaguchi, P. Zapol, H. You, D. Tripkovic, D. Strmcnik, Y. Zhu, S. Seifert, S. Lee, V. R. Stamenkovic and N. M. Markovic, *Nat. Energy*, 2020, **5**, 222–230.

33 R. Gisbert, G. García and M. T. M. Koper, *Electrochim. Acta*, 2010, **55**, 7961–7968.

34 G. Niaura, A. K. Gaigalas and V. L. Vilker, *J. Phys. Chem. B*, 1997, **101**, 9250–9262.

35 Y. Zhang, X. Zhang, S. Chen, J. Liu, T. Li, L. Wang and K. Wu, *Corros. Commun.*, 2023, **9**, 77–88.

36 R. M. Smith and A. E. Martell, *Critical Stability Constant: Inorganic Complexes*, vol.4, 1976, pp. 56–57.

37 R. Priambodo, Y. J. Shih and Y. H. Huang, *RSC Adv.*, 2017, **7**, 40819–40828.

38 D. Rai, D. A. Moore, N. J. Hess, L. Rao and S. B. Clark, *J. Solution Chem.*, 2004, **33**, 1213–1242.

39 S. M. Aboufaris EL Alaoui, L. Ghallali, M. EL Guendouzi and A. Benbiyi, *J. Solution Chem.*, 2022, **51**, 802–815.

40 A. Fukunaga and K. Zhao, *J. Surf. Finish. Soc. Japan*, 2021, **72**, 443–449.

41 T. Fujino, N. Fukumuro, M. Ida, Y. Ida and S. Yae, *J. Surf. Finish. Soc. Japan*, 2021, **72**, 560–566.

42 M. Pourbaix, *Mater. Sci. Forum*, 1997, **251–254**, 143–148.